

LATE-TIME X-RAY, UV AND OPTICAL MONITORING OF SUPERNOVA 1979C

STEFAN IMMLER¹, ROBERT A. FESEN², SCHUYLER D. VAN DYK³, KURT W. WEILER⁴, ROBERT PETRE¹, WALTER H. G. LEWIN⁵, DAVID POOLEY⁶, WOLFGANG PIETSCH⁷, BERND ASCHENBACH⁷, MOLLY C. HAMMELL² AND GWEN C. RUDIE²

Draft version August 3, 2021

ABSTRACT

We present results from observations of SN 1979C with *XMM-Newton* in X-rays and in the UV, archival X-ray and *HST* data, and follow-up ground-based optical imaging. The *XMM-Newton* MOS spectrum shows best-fit two-temperature thermal plasma emission characteristics of both the forward ($kT_{\text{high}} = 4.1^{+76}_{-2.3}$ keV) and reverse shock ($kT_{\text{low}} = 0.78^{+0.25}_{-0.17}$ keV) with no intrinsic absorption. The long-term X-ray lightcurve, constructed from all X-ray data available, reveals that SN 1979C is still radiating at a flux level similar to that detected by *ROSAT* in 1995, showing no sign of a decline over the last six years, some 16–23 yrs after its outburst. The high inferred X-ray luminosity ($L_{0.3-2} = 8 \times 10^{38}$ ergs s⁻¹) is caused by the interaction of the SN shock with dense circumstellar matter, likely deposited by a strong stellar wind from the progenitor with a high mass-loss rate of $\dot{M} \approx 1.5 \times 10^{-4} M_{\odot} \text{ yr}^{-1}$ ($v_w/10 \text{ km s}^{-1}$). The X-ray data support a strongly decelerated shock, and show a mass-loss rate history which is consistent with a constant progenitor mass-loss rate and wind velocity over the past $\gtrsim 16,000$ yrs in the stellar evolution of the progenitor. We find a best-fit CSM density profile of $\rho_{\text{CSM}} \propto r^{-s}$ with index $s \lesssim 1.7$ and high CSM densities ($\gtrsim 10^4 \text{ cm}^{-3}$) out to large radii from the site of the explosion ($r \gtrsim 4 \times 10^{17} \text{ cm}$). Using *XMM-Newton* Optical Monitor data we further detect a point-like optical/UV source consistent with the position of SN 1979C, with *B*, *U*, and *UVW1*-band luminosities of 5, 7, and 9×10^{36} ergs s⁻¹, respectively. The young stellar cluster in the vicinity of the SN, as imaged by the *HST* and follow-up ground-based optical imaging, can only provide a fraction of the total observed flux, so that a significant contribution to the output likely arises from the strong interaction of SN 1979C with dense CSM.

Subject headings: stars: supernovae: individual (SN 1979C) — stars: circumstellar matter — galaxies: individual (M100, NGC 4321) — X-rays: general — X-rays: individual (SN 1979C, M100, NGC 4321) — X-rays: ISM — ultraviolet: ISM

1. INTRODUCTION

The interaction of the outgoing supernova (SN) shock and ejecta with the circumstellar medium (CSM) can produce substantial amounts of X-ray emission. The dominant X-ray production mechanism is the interaction of the SN shock with the ambient CSM deposited either by a pre-SN stellar wind or non-conservative mass transfer to a companion. This interaction produces hot gas with a characteristic temperature in the range $T \sim 10^7$ – 10^9 K (Chevalier & Fransson 1994). Gas heated to such a high temperature produces radiation predominantly in the X-ray range. X-ray emission from this interaction is expected for all Type Ib/c and II SNe with substantial CSM established by the massive progenitors. The details of the CSM interaction are dis-

cussed in Fransson, Lundqvist & Chevalier (1996) and references therein, while the X-ray interaction luminosity is briefly summarized here (see also Immler & Lewin 2003): the thermal X-ray luminosity, L_x , produced by the shock heated CSM, can be expressed as $L_x = 4/(\pi m^2) \Lambda(T) \times (\dot{M}/v_w)^2 \times (v_s t)^{-1}$, where m is the mean mass per particle (2.1×10^{-27} kg for a H+He plasma), $\Lambda(T)$ the cooling function of the heated plasma at temperature T , \dot{M} the mass-loss rate of the progenitor, v_w the speed of the stellar wind blown off by the progenitor, and v_s the speed of the outgoing shock. If X-ray spectroscopic data are available, $\Lambda(T)$ is known, and the interaction luminosity L_x at time t after the outburst can be used to measure the ratio \dot{M}/v_w . Assuming a constant SN shock velocity v_s , the shock will reach a radius of $r = v_s t$ from the site of the explosion at time t after the explosion.

If the CSM density ρ_{CSM} is dominated by a wind from the progenitor of the SN, the continuity equation requires $\dot{M} = 4\pi r^2 \rho_w(r) \times v_w(r)$ through a sphere of radius r , where ρ_w is the stellar wind density. After the SN shock plows through the CSM, its density is $\rho_{\text{CSM}} = 4\rho_w$ (Fransson, Lundqvist & Chevalier 1996), assuming no losses to cosmic ray acceleration.

Since each X-ray measurement at time t is related to the corresponding distance r from the site of the explosion, which has been reached by the wind at a time depending on v_w , or the age of the wind $t_w = tv_s/v_w$, we can use our measurements as a ‘time machine’ to probe

¹ Exploration of the Universe Division, X-Ray Astrophysics Laboratory, Code 662, NASA Goddard Space Flight Center, Greenbelt, MD 20771, USA

Electronic address: immler@milkyway.gsfc.nasa.gov

² Department of Physics and Astronomy, 6127 Wilder Laboratory, Dartmouth College, Hanover, NH 03755, USA

³ Spitzer Science Center/Caltech, 220-6, Pasadena, CA 91125, USA

⁴ Naval Research Laboratory, Code 7213, Washington, DC 20375-5320, USA

⁵ Center for Space Research, Massachusetts Institute of Technology, 77 Massachusetts Avenue, Cambridge, MA 02139, USA

⁶ Department of Astronomy, University of California, 601 Campbell Hall, Berkeley, CA 94720-3411, USA

⁷ Max-Planck-Institut für extraterrestrische Physik, PO Box 1312, 85741 Garching bei München, Germany

the progenitor’s history over significant time scales. Assuming that v_w and v_s did not change over t_w , or in cases where the shock front deceleration is known from radio data, we can even directly measure the mass loss rate back in time. Furthermore, integration of the mass-loss rate along the path of the expanding shell gives the mean density inside a sphere of radius r . For a constant wind velocity v_w and constant mass-loss rate \dot{M} , a $\rho_{\text{CSM}} = \rho_0(r/r_0)^{-s}$ profile with $s = 2$ is expected.

After the expanding shell has become optically thin, it is expected that emission from the SN ejecta itself, heated by the reverse shock, dominates the X-ray output of the interaction regions due to its higher emission measure and higher density. Since the plasma temperature of the ejecta is lower than that of the shocked CSM, a significant ‘softening’ of the X-ray spectrum is expected (e.g., Chevalier & Fransson 1994; Fransson, Lundqvist & Chevalier 1996).

The number of detected X-ray SNe has substantially grown over the past few years. With 22 detections to date⁸ and high-quality X-ray spectra available from *XMM-Newton* and *Chandra* observations, a wealth of new information has been gathered (see Immler & Lewin 2003 for a review article).

The signatures of circumstellar interaction in the radio, optical, and X-ray regimes have been found for a number of core-collapse SNe, such as the Type II-L SN 1979C (e.g., Weiler et al. 1986, 1991; Fesen & Matonick 1993; Immler et al. 1998). SN 1979C was discovered in the optical near maximum light on April 19, 1979 (Johnson 1979), and detected in X-rays 16 yrs after its outburst with the *ROSAT* HRI, with a luminosity of $L_{0.1-2.4} = 1.3 \times 10^{39}$ ergs s⁻¹ (Immler et al. 1998). The *ROSAT* data imply a mass-loss rate of $\dot{M} \sim 1 \times 10^{-4} M_{\odot} \text{ yr}^{-1}$ ($v_w/10 \text{ km s}^{-1}$), similar to the mass-loss rates of other massive ($\gtrsim 10 M_{\odot}$) SN progenitors (e.g. SNe 1978K, 1986J, 1988Z, and 1998S) and in agreement with the mass-loss rate inferred from VLA radio observations ($\dot{M} = 1.2 \times 10^{-4} M_{\odot} \text{ yr}^{-1}$ [$v_w/10 \text{ km s}^{-1}$]; Weiler et al. 1991). Earlier *Einstein* observations only gave an upper limit to the X-ray luminosity on days 64, 239, and 454 after the outburst, with 3σ upper limits of 1.8×10^{40} ergs s⁻¹, 7.6×10^{39} ergs s⁻¹ and 6.9×10^{39} ergs s⁻¹, respectively (Immler et al. 1998). Since the *ROSAT* HRI instrument does not provide energy information, and subsequent *ASCA* and *Chandra* observations (Kaaret 2001; Ray, Petre & Schlegel 2001) lacked enough photon statistics for X-ray spectroscopy, there is no information about the X-ray spectral properties of SN 1979C and thus the temperatures of the forward and reverse shock.

SN 1979C was extensively monitored in the radio starting eight days after maximum light, and showed an initial rate of decline of $t^{-0.7}$ (Weiler et al. 1986, 2001), followed by a flattening or possibly brightening at an age of ≈ 10 yrs, while maintaining a relatively constant spectral index (Montes et al. 2000; Weiler et al. 2001). The results were interpreted as being due to a denser region in the CSM or a complex CSM structure which might have been modulated by the stellar wind of the progenitor’s companion (Weiler et al. 1992).

There are conflicting reports in the literature regarding the expansion velocity of the ejecta. While Bartel & Bietenholz (2003) find a near-free expansion (i. e., $E(T, V) = [\text{const.}]$) based on VLBI data from $t = 3.7$ –22 yrs after the explosion, Marcaide et al. (2002) report the detection of a strongly decelerated expansion. There is consensus, however, that the initial expansion of the shock over the first 6 ± 2 yrs was free, with $v_s \approx 9,000 \text{ km s}^{-1}$ (see Marcaide et al. 2002 and references therein). The claimed onset of the deceleration to $v_s \approx 6,200 \text{ km s}^{-1}$ coincides with the flattening of the radio lightcurve and might be indicative for the shock running into a dense CSM (Marcaide et al. 2002).

Low-dispersion Keck optical spectra obtained at $t = 14.8$ yrs and 17 yrs, as well as *HST* UV spectra 17 yrs after the outburst revealed broad $\approx 6,000 \text{ km s}^{-1}$ emission lines, as well as blueward peaks which are substantially stronger than those toward the red, indicating internal dust extinction within the expanding ejecta. Profile differences between hydrogen and oxygen line emission suggest two or more separate emitting regions, such as a H α bright shell and oxygen inner ejecta region (Fesen et al. 1999).

HST imaging of the SN 1979C environment showed the presence of a cluster of stars in the vicinity of SN 1979C, containing both young (≈ 4 –8 Myrs) blue stars, as well as older red supergiants (≈ 20 Myrs), and succeeded in identifying SN 1979C as the brightest source in the optical and UV in that cluster (van Dyk et al. 1999). The data were further used to estimate the mass of the progenitor to be $18 \pm 3 M_{\odot}$, in agreement with a mass-estimate derived from radio data ($\gtrsim 13 M_{\odot}$, Weiler et al. 1991).

In this paper we report on *XMM-Newton* X-ray and UV observations of SN 1979C, all archival X-ray data available, as well as archival *HST* images and new ground-based optical data. In §2 we describe the data and analysis thereof and report on the X-ray spectrum, multi-mission X-ray lightcurve, UV photometry, and new follow-up ground-based optical imaging in §3. We discuss the results in the context of the CSM interaction model and compare them to other core-collapse SNe in §4, followed by a brief summary in §5.

2. DATA PROCESSING AND ANALYSIS

SN 1979C and its host galaxy NGC 4321 (M100) were observed with *XMM-Newton* as part of a GTO program on December 28, 2001, with the EPIC PN instrument for 31.6 ks, and the EPIC MOS1 and MOS2 instruments for 36.2 ks and 36.0 ks, respectively, using the medium filter. Data processing and analysis were performed with SAS 6.1 and the latest calibration constituents, as well as FTOOLS and own IDL routines. Spectral fitting was performed using XSPEC 11.3.1.

In order to establish the long-term X-ray lightcurve of SN 1979C we further extracted and reduced all X-ray data available in the archives (see §2.3). *XMM-Newton* Optical Monitor data of SNe 1979C (§2.2), as well as archival *HST* and recent MDM observations (§2.4) were further used to estimate optical/UV fluxes.

2.1. XMM-Newton EPIC Data

Screening of the PN and MOS data for periods with a high background revealed contamination of the data

⁸ A complete list of X-ray SNe and references are available at http://lheawww.gsfc.nasa.gov/users/immler/supernovae_list.html

at the end of the observation period. Exclusion of these flaring periods gave cleaned exposure times of 27.1 ks (PN) and 23.6 ks (MOS).

Inspection of the EPIC images further showed that the position of SN 1979C coincides with a chip gap on the PN detector, making a reliable count rate estimate impossible. The PN data were therefore not used in the analysis and we will restrict ourselves to the EPIC MOS data only. The MOS data were further screened using the parameters “FLAG=0” and “PATTERN ≤ 12 ” and filtered to retain the 0.3–10 keV energy band only in order to avoid contamination from soft-proton flaring and uncertainties in the calibration at low energies. The merged 0.3–10 keV band MOS1+MOS2 image of M100/SN 1979C is shown in the left-hand panel of Fig. 1. MOS counts were extracted within a circle of radius $30''$ centered on the radio position of SN 1979C and corrected for the energy-enclosed aperture. The background was estimated locally from a source-free annulus with inner and outer radii of $45''$ and $55''$, respectively, to account for residual diffuse emission from the host galaxy.

2.2. XMM-Newton Optical Monitor Data

Optical Monitor (OM) data were obtained in 16 individual exposures in the *B*-band (effective wavelength $4,340 \text{ \AA}$), *U*-band ($3,440 \text{ \AA}$), and *UVW1*-band ($2,910 \text{ \AA}$), with on-source exposure times of 2.0 ks (*B*), 1.8 ks (*U*), and 1.9 ks (*UVW1*). OM data were reprocessed using the SAS “omichain” task, and following the data analysis threads in the ABC Guide version 2.01⁹.

For imaging and source detection, the tracking history was created, bad pixels were removed, a flat field generated, and images were corrected for “modulo-8” spatial fixed-pattern noise. Source detection was performed using the “omdetect” task, which employs a two-stage process to locate sources in OM Science Window images, i.e., determination of the background and consecutive island search (“box detect”) in which sets of pixels above the sigma significance cut-off are identified and grouped into individual objects. Source counts were converted into instrument-bandpass magnitudes utilizing the “ommag” command. Fluxes were converted from count rates using a step-by-step recipe provided by Alice Breeveld¹⁰. We also employed the interactive “omsources” task with various aperture sizes to verify the magnitudes obtained with “omichain” and to check for potential contamination of the OM photometry with nearby sources.

Comparison of the optical positions of six stars from the Guide Star Catalog with the centroid positions of the stars in the *B*, *U*, and *UVW1* images revealed an offset of individual OM images of $\Delta\text{R.A.} = 0''.14$ and $\Delta\text{Dec.} = -0''.95$ (*B*), $\Delta\text{R.A.} = 0''.43$ and $\Delta\text{Dec.} = -1''.75$ (*U*), and $\Delta\text{R.A.} = 1''.01$ and $\Delta\text{Dec.} = -2''.23$ (*UVW1*). This offset was also visible in an overlay of the *B*, *U*, and *UVW1* images. After re-alignment of the images with shifts in R.A. and Dec. as quoted above, no systematic offset between the different images, and no statistically significant offset between the centroid positions of the stars with the Guide Star Catalog positions are observed.

A three-color (*B*, *U*, *UVW1*) image of M100 and SN 1979C is shown in the right-hand panel of Fig. 1. The

circular enhancement in the south-western spiral arm of M100, most prominent in the *B*-band image (color-coded in red), is due to stray-light from the bright nucleus of M100. Due to its large offset from the position of SN 1979C and local background extraction, however, it does not affect the SN 1979C photometry. An XMM-Newton OM *U*-band image of the region around the position of SN 1979C is further shown in more detail in Fig. 2 (upper panel).

2.3. Other X-Ray Data

In addition to the XMM-Newton data described above, we used archival data from *Einstein* (HRI), *ROSAT* (HRI and PSPC), *ASCA* (SIS), and a recent *Chandra* (ACIS-S) observation. All *Einstein* observations were merged into a single 41.2 ks observation to increase the photon statistics. Count rates from the archival *Einstein* HRI and *ROSAT* HRI observations were taken from Immler et al. (1998), *Chandra* count rates were taken from Ray, Petre & Schlegel (2001) and Kaaret (2001), and *ASCA* upper limits from Ray, Petre & Schlegel (2001). We further extracted source counts for each of these observations following standard analysis methods as described in the respective instrument handbooks using FTOOLS to check and reproduce published count rates. Two previously unpublished *ROSAT* HRI observations were analyzed as described in Immler et al. (1998).

A *ROSAT* PSPC observation from December 8, 1998, was also used to establish the long-term X-ray lightcurve of SN 1979C. This observation was selected as part of the *ROSAT* PSPC “last-light” campaign during which the PSPC instrument was re-activated for a final set of observations just days before *ROSAT* was decommissioned. Inspection of the PSPC data showed that the position of SN 1979C was sufficiently offset from the “gain hole” which emerged on the PSPC-B detector images taken during the short “last-light” campaign. Exposure corrected counts were extracted from the position of SN 1979C within a circle of radius $30''$ and corrected for the 100% encircled energy radius. The background was estimated locally within an annulus of inner and outer radii of $1'$ and $1\frac{1}{3}'$. The net exposure time of the observation is 7.8 ks. A log of all X-ray observations utilized in this paper is given in Table 1.

2.4. Follow-up Ground-based Optical Imaging

$\text{H}\alpha$ and *R*(Harris)-band images were obtained at the MDM Observatory on December 19 and 20, 2004 (epoch = $2004.97 \simeq 2005.0$), using the Hiltner 2.4 m telescope and the Columbia 8K CCD camera (Crotts 2001). The images were used to investigate further the nature of the source detected at the SN 1979C site, and to compare more directly its current optical flux level with that seen in previous late-time optical detections (Fesen et al. 1999; van Dyk et al. 1999). Two 1,000 s *R*-band and three 1,000 s $\text{H}\alpha$ exposures binned 2×2 yielding an image scale of $0.404 \text{ arcsec/pixel}$ were taken under poor to fair conditions. The $\text{H}\alpha$ image had poor image quality ($3''$ FWHM) while the *R*-band images were fair to good ($1\frac{1}{2}$ – $1\frac{1}{4}''$ FWHM). These data were reduced, co-added and cosmic ray corrected using standard IRAF software routines. The MDM *R*-band image of the region around the position of SN 1979C is shown in Fig. 2 (lower panel).

⁹ available from <http://heasarc.gsfc.nasa.gov/docs/xmm/abc/>

¹⁰ available from <http://xmm.vilspa.esa.es/sas/documentation/watchdog.html>

As a means for comparison of current optical flux levels, we also retrieved and reprocessed the archival *HST* WFPC-PC1 images of the SN 1979C region (c.f. van Dyk et al. 1999). These data consist of several filter images taken July 29, 1996, using the WFPC2 camera with the SN 1979C site centered in the high resolution Planetary Camera (PC1; 0.046 arcsec/pixel). Two 500 s broadband red (F675W), three 1,300 s H α (F658N), two 1,200 s *B*-band (F439W), and two 1,300 s *U*-band (F336W) filter images were co-added and cosmic rays removed via high pixel value rejection procedure. A few obvious residual cosmic ray contaminated pixels on the summed F675W image were also removed manually using the IRAF software package “tv.imedit”. All optical/UV observations utilized in this paper are listed in Table 2.

3. RESULTS

3.1. X-Ray Data

SN 1979C is detected in the MOS images with a count rate of $(3.6 \pm 0.5) \times 10^{-3}$ cts s $^{-1}$, 23 yrs after its outburst. Simultaneous spectral fitting of the MOS data in the 0.5–8 keV band gives a best-fit (reduced $\chi_r^2 = 0.65$ for 18 degrees of freedom) two-temperature plasma emission model (XSPEC model ‘MEKAL’) with $kT_{\text{low}} = 0.77_{-0.19}^{+0.17}$ keV and $kT_{\text{high}} = 2.31_{-0.66}^{+1.95}$ keV, and a best-fit absorbing column density of $N_{\text{H}} = 2.53_{-2.53}^{+4.96} \times 10^{20}$ cm $^{-2}$ consistent with the Galactic foreground column density ($N_{\text{H}} = 2.39 \times 10^{20}$ cm $^{-2}$; Dickey & Lockman 1990). Element abundances cannot be constrained due to the low photon statistics. In order to avoid contamination of the spectra with unresolved and hard XRBs within the disk of M100, we further fitted the spectrum in the 0.5–2 keV band, where the bulk of emission from the reverse shock is expected. A best-fit two-temperature thermal plasma emission model ($\chi_r^2 = 0.61$, d.o.f = 8) gives $kT_{\text{low}} = 0.78_{-0.17}^{+0.25}$ keV and $kT_{\text{high}} = 4.1_{-2.3}^{+76}$ keV, and an absorbing column density of $N_{\text{H}} = 0\text{--}1.01 \times 10^{21}$ cm $^{-2}$. Adopting this spectral template gives 0.3–2 keV and 2–8 keV fluxes of $f_{0.3-2} = 2.31 \times 10^{-14}$ ergs cm $^{-2}$ s $^{-1}$ and $f_{2-8} = 1.81 \times 10^{-14}$ ergs cm $^{-2}$ s $^{-1}$, respectively. The soft component contributes 64% to the total emission, while the hard component accounts for the remaining 36% of the 0.3–2 keV band flux. The MOS spectra and best-fit model are shown in Fig. 3.

A single component thermal plasma spectrum gives best-fit $kT = 0.60_{-0.19}^{+0.12}$ keV and an absorbing column density of $N_{\text{H}} = 6.5_{-1.9}^{+2.0} \times 10^{21}$ cm $^{-2}$ ($\chi_r^2 = 1.29$, d.o.f = 11). Using these spectral properties gives a soft-band flux of $f_{0.3-2} = 1.69 \times 10^{-14}$ ergs cm $^{-2}$ s $^{-1}$. A thermal bremsstrahlung spectrum with $kT = 0.53_{-0.33}^{+1.40}$ keV ($\chi_r^2 = 0.91$, d.o.f = 11) cannot be statistically ruled out, but shows significantly larger systematical offsets from the observed spectrum, especially at lower energies. Adopting this spectral template gives a soft-band flux of $f_{0.3-2} = 2.11 \times 10^{-14}$ ergs cm $^{-2}$ s $^{-1}$. Other spectral models, such as a power-law ($\Gamma = 4.48_{-0.48}^{+0.53}$; $\chi_r^2 = 0.87$, d.o.f = 17) or a non-equilibrium ionization model ($kT = 73.4_{-33.0}^{+6.5}$ keV; $\chi_r^2 = 0.93$, d.o.f = 16) cannot be statistically ruled, but give unreasonable physical parameters.

Using the above two-temperature thermal plasma spectral template and assuming a distance of 17.1 Mpc

(Freedman et al. 1994), we infer soft- and hard-band X-ray luminosities of $L_{0.3-2} = 8 \times 10^{38}$ ergs s $^{-1}$ and $L_{2-10} = 3 \times 10^{38}$ ergs s $^{-1}$, respectively.

We also analyzed the multi-mission data set to construct the long-term X-ray lightcurve of SN 1979C, using the same spectral template to convert count rates into fluxes and luminosities. The long-term X-ray lightcurve is shown in Fig. 4. We calculated the mass-loss rate of the progenitor as a function of age of the stellar wind assuming a constant shock velocity of 9,200 km s $^{-1}$ (Marcaide et al. 2002). An effective (0.3–2 keV band) cooling function of $\Lambda = 3 \times 10^{-23}$ ergs cm 3 s $^{-1}$ for an optically thin thermal plasma with a temperature of 10^7 K was adopted, which corresponds to the temperature inferred from the MOS spectra. Adopting different plasma temperatures in the range 0.5–1 keV would lead to changes in the emission measure of $\approx 10\%$. This error in the emission measure is included in calculations of the CSM number densities (§ 4.1). Key physical properties of SN 1979C are listed in Table 3.

While the mass-loss rate history (see Table 3 and left-hand panel of Fig. 5) indicates a slight increase in the mass-loss rate toward a larger stellar wind age, the results are not statistically significant. We further calculated the mass-loss rate history assuming a strongly decelerated expansion of the shock of 9,200 km s $^{-1}$ for a stellar wind age of $t_{\text{w}} < 6$ yrs, 6,200 km s $^{-1}$ for $6 \text{ yrs} < t_{\text{w}} < 14$ yrs, and 5,400 km s $^{-1}$ for $t_{\text{w}} > 20$ yrs, corresponding to a deceleration $R \propto t^m$ with a deceleration parameter of $m = 0.6$ (Marcaide et al. 2002) to approximate a continually decelerating shock. The results are shown in the right-hand panel of Fig. 5. The introduction of a deceleration leads to a constant mass-loss rate of $\dot{M} \approx 1.5 \times 10^{-4} M_{\odot}$ yr $^{-1}$ ($v_{\text{w}}/10$ km s $^{-1}$).

We computed the CSM number density in the vicinity of the SN by integrating the mass-loss rate within the sphere probed by the CSM interaction. The post-shock CSM number densities, $n = \rho_{\text{CSM}}/m$, for the different radii $r = v_{\text{s}}t$ corresponding to the dates of the observations, are listed in Table 3. An overall decrease in the CSM density is observed from $n = (1.17 \pm 0.32) \times 10^4$ cm $^{-3}$ at $\log r[\text{cm}] = 17.50$ (ROSAT HRI) to $n = (0.85 \pm 0.19) \times 10^4$ cm $^{-3}$ at $\log r[\text{cm}] = 17.59$ (XMM-Newton), albeit not statistically significant. While the ROSAT PSPC and *Chandra* data at $\log r[\text{cm}] = 17.52$ ($n = [1.66 \pm 0.63] \times 10^4$ cm $^{-3}$) and 17.53 cm ($n = [1.51 \pm 0.56] \times 10^4$ cm $^{-3}$) are slightly higher, they are consistent with the earlier ROSAT HRI and later XMM-Newton data within the errors. The CSM density profile will be discussed in more detail in § 4.1.

3.2. XMM-Newton Optical Monitor Data

An optical/UV source is found at the position of SN 1979C in the *B*, *U*, and *UVW1* bands, with magnitudes of $m_{\text{B}} = (19.1 \pm 0.1)$ mag, $m_{\text{U}} = (18.0 \pm 0.1)$ mag, and $m_{\text{UVW1}} = (17.6 \pm 0.1)$ mag, and source detection significances of 17.1σ , 28.1σ , and 34.5σ , respectively, within an aperture of 12 pix ($4''.1$ FWHM). The source is flagged as point-like by the source detection algorithm. Magnitudes were converted into fluxes with Vega as a reference (Vega has magnitudes of $m_{\text{B}} = 0.030$ mag, and $m_{\text{U}} = m_{\text{UVW1}} = 0.035$ mag), and a relation of $m_{\text{Vega}} - m_{\text{SN1979C}} = -2.5 \log(f_{\text{Vega}}/f_{\text{SN1979C}})$, and Vega

fluxes in the OM B , U , and $UVW1$ filters of 5.97, 3.15, and 3.73×10^{-9} ergs cm $^{-2}$ s $^{-1}$ Å $^{-1}$. We obtain B , U , and $UVW1$ band fluxes for SN 1979C of 1.4, 2.0, and 3.3×10^{-16} ergs cm $^{-2}$ s $^{-1}$ Å $^{-1}$, respectively.

In order to minimize contamination of the optical/UV with potential unresolved neighboring sources, we also extracted OM counts within smaller apertures of 3 pixel radius (2''.9) from the centroid position of SN 1979C. Using this small aperture we obtain $m_{UVW1} = (17.9 \pm 0.1)$ mag, $f_{UVW1} = 2.6 \times 10^{-16}$ ergs cm $^{-2}$ s $^{-1}$ Å $^{-1}$, and $L_{UVW1} = 9.0 \times 10^{36}$ ergs s $^{-1}$.

3.3. R -Band and $H\alpha$ Imaging

Our 2005.0 MDM R -band image of the SN 1979C region in M100 is shown in Figs. 2 and 7, along with the 2002.0 *XMM-Newton* OM U -band image, and the 1996.6 *HST* WFPC-PC1 red (F675W), $H\alpha$ (F658N), B -band (F439W), and U -band (F336W) images. The MDM R -band image shows a bright source at the position of SN 1979C with a strength that suggests little change in R -band luminosity from that seen in the 1996.6 *HST* F675W images. Although the WFPC2 F675W and R (Harris) bandpasses are different in wavelength coverage (F675W bandpass: 6,000–7,500 Å; R (Harris) bandpass: 5,600–8,200 Å), they are both about equally sensitive to the strong and broad emission lines of [O I] $\lambda\lambda 6300, 6364$, $H\alpha$, and [O II] $\lambda\lambda 7319, 7330$ which dominate the late-time spectrum of SN 1979C (Fesen et al. 1999). This permits one to roughly equate these two filter images for purposes of comparing total emission line levels in SN 1979C.

Relative flux measurements on the WFPC2-PC1 F675W and MDM R -band images of the SN 1979C source and several surrounding point sources, including the bright source 2''0 nearly due east, were taken and indicate SN 1979C's 2005.0 6,000–7,500 Å flux has remained constant to ± 0.25 mag from its 1996.6 level. Concerning the current level of $H\alpha$ flux, the poor image quality of the MDM $H\alpha$ image, differences in filter passbands between the WFPC2/F658N ($\lambda_0 = 6,591$ Å; FWHM = 29 Å) and the MDM 8K/ $H\alpha$ filter ($\lambda_0 = 6,565$ Å; FWHM = 80 Å), plus uncertainty as to the association of a strong, narrow $H\alpha$ at the rest frame velocity of M100 ($v = 1,570$ km s $^{-1}$) with SN/CSM interaction make a definitive statement difficult. Nonetheless, the ground-based image data do suggest that considerable $H\alpha$ emission currently exists at the SN 1979C site at a level consistent with that seen in the 1996.0 WFPC2-PC1 image (see Fig. 7, right-hand panel).

4. DISCUSSION

4.1. X-Ray Data

SN 1979C is detected at a high flux level 23 yrs after its outburst, with no indication of a decline over the last six years. This is in stark contrast to most other X-ray SNe which typically show X-ray and radio rates of decline of $L_x \propto t^n$ with index n in the range 0.3–1.4 (see Immler & Lewin 2003 and Sramek & Weiler 2003 for review articles of the X-ray and radio rates of decline). The only SN which shows a similar persistent X-ray lightcurve is SN 1978K (Schlegel et al. 1999, 2004). Clearly, the high inferred flux is indicative of large amounts of shocked

CSM and a high mass-loss rate in the scenario of the CSM being deposited by the progenitor.

Furthermore, our analysis may indicate a possible increase of the mass-loss rate for larger stellar wind ages (see left-hand panel of Fig. 5) if we assume a constant velocity forward shock. In order to check whether incorrect assumptions in the spectral properties of SN 1979C might mimic such an increase of the mass-loss rate, we investigated the effect of the assumed spectral parameters used for the conversion of source counts into fluxes. However, given our observed MOS count rates, we cannot find spectral templates with realistic plasma temperatures which could account for the apparent increase in the mass-loss rate. In fact, if we adopt a spectral template which only includes a hard thermal component with 10 keV for the forward shock emission for the earlier data for which no spectral information is available, the inferred flux would be 37% lower when compared to our two-temperature thermal emission model, which takes the emergence of the (softer) reverse shock into account. We therefore can not reproduce a flat mass-loss rate history by changing the plasma temperatures of the shocked CSM alone.

Instead, we find that the mass-loss rate history is best represented by a constant stellar wind velocity and constant mass-loss rate by assuming that the shock front experienced a strong deceleration. Adopting deceleration parameters derived from VLBI imaging (with 9,200 km s $^{-1}$ for $t_w < 6$ yrs, 6,200 km s $^{-1}$ for 6 yrs $< t_w < 14$ yrs, and 5,400 km s $^{-1}$ for $t_w > 20$ yrs; Marcaide et al. 2002) gives a flat (slope = 0) mass-loss rate history (see right-hand panel of Fig. 5). This indicates that the assumed deceleration parameters are indeed plausible, and contradict claims for a free expansion based on the same VLBI data (Bartel & Bietenholz 2003).

The early upper limit from the merged *Einstein* data 0.66 yrs after the outburst, however, is in conflict with a constant stellar wind velocity and constant mass-loss rate model (see Fig. 5). Similarly to SN 1979C, an early ROSAT upper limit to the X-ray flux of the SN Ic 1994I on day 52 has been reported to be in conflict with the X-ray evolution in terms of a simple power-law, and with a constant mass-loss rate and wind velocity (Immler et al. 2002). This is indicative that a simple power-law model for the X-ray rate of decline might be incomplete for describing the early epoch in the CSM interaction. Assuming an initial exponential rise of the X-ray luminosity after the outburst (at time t_0) and a subsequent power-law decline with index s , we can parameterize the X-ray evolution as $f_x \propto (t - t_0)^{-s} \times e^{-\tau}$ with $\tau \propto (t - t_0)^{-\beta}$. This model has been successfully used to describe the time dependence of the radio emission of SNe (Weiler et al. 1986) and the X-ray emission of SN 1994I (Immler et al. 2002). In this representation the external absorption of the emission is represented by the $e^{-\tau}$ term ('optical depth') and the time-dependence of the optical depth is parameterized by the exponent β . The rise of the X-ray flux could be either due to a decreasing absorption by intervening material along the line-of-sight to the X-ray emitting hot gas or could simply indicate a non-production of soft X-rays at early times. Unfortunately, the lack of high-quality data for SN 1979C at early times precludes a more detailed investigation. The

low inferred mass-loss rate around 0.66 yrs after the outburst of SN 1979C, however, could be due to such an exponential increase in the X-ray emission. The data can therefore be reconciled with a constant mass-loss rate history if we assume an initial rise of the emission, which is observationally not further constrained.

Long-term X-ray lightcurves and high-quality spectra are also available for SNe 1993J (Immler et al. 2001; Zimmermann & Aschenbach 2003) and 1978K (Schlegel et al. 2004). While the overall X-ray lightcurve of SN 1993J is best described by a $t^{-0.3}$ rate of decline, significant ‘bumps’ around day $\approx 1,000$ are observed, which might be due to a change in the slope of the CSM density profile (Zimmermann & Aschenbach 2003). VLBI imaging revealed that the expanding shock region has a circular morphology, which is indicative of a smooth CSM. Based on the X-ray and radio data, a significant change in the mass-loss rate of the SN 1993J progenitor was discovered, with a continuous decrease from $\dot{M} = 4 \times 10^{-4} M_{\odot} \text{ yr}^{-1}$ to $4 \times 10^{-5} M_{\odot} \text{ yr}^{-1}$ during the late stages of the evolution (Immler et al. 2001; van Dyk et al. 1994). This evolution has been interpreted as a transition in the progenitor’s evolution from the red to the blue supergiant phase during the last $\approx 10,000$ yrs of the evolution (Immler et al. 2001). While a deceleration of the shock could not account for the change in the mass-loss rate history for SN 1993J, correction for a strongly decelerated shock produces a flat mass-loss rate history for SN 1979C with $\dot{M} \approx 1.5 \times 10^{-4} M_{\odot} \text{ yr}^{-1} (v_w/10 \text{ km s}^{-1})$. The bumpy CSM structure inferred for SN 1979C based on our analysis might be largely explained by systematic and statistical uncertainties in the X-ray flux, especially when the cross-calibration uncertainties between *Einstein*, *ROSAT*, *Chandra*, and *XMM-Newton* are taken into account (which would add an additional $\lesssim 10\%$ to the errors quoted in this paper; see Snowden 2002 and the EPIC Calibration Documentation¹¹). We therefore conclude that SN 1979C does not show any evidence for a change in the stellar wind parameters.

The X-ray spectrum of SN 1979C is best described by a two-temperature thermal plasma emission model with $kT_{\text{low}} = 0.78^{+0.25}_{-0.17} \text{ keV}$, $kT_{\text{high}} = 4.1^{+76}_{-2.3} \text{ keV}$, accounting for 64% and 36% of the total (0.3–2 keV) flux, respectively, and no intrinsic absorption. Single-component fits cannot be statistically excluded and give a similar temperature ($kT = 0.60^{+0.12}_{-0.19} \text{ keV}$ for a thermal plasma fit; $kT = 0.53^{+1.40}_{-0.33} \text{ keV}$ for a thermal bremsstrahlung fit) and flux compared to the soft component of the two-temperature fit. The hard and soft spectral components are likely due to emission from the forward (hard component) and reverse shock (soft component). While minor contamination of the spectrum with unresolved XRBs within the disk of M100 cannot be conclusively excluded, spectral analysis of various point-source free regions within the D_{25} ellipse of M100 give plasma temperatures significantly different from the spectral components above ($kT = [0.13 \pm 0.08] \text{ keV}$) and likely originate in hot plasma within or above the disk of M100.

Similarly to SN 1979C, a best-fit two-temperature thermal plasma model with $kT_{\text{low}} = (0.34 \pm 0.04) \text{ keV}$ and $kT_{\text{high}} = (6.54 \pm 4) \text{ keV}$ was observed for SN 1993J based

on high-quality *XMM-Newton* spectroscopy eight years after its outburst (Zimmermann & Aschenbach 2003). While these temperatures differ from the plasma temperatures found for SN 1979C ($kT_{\text{low}} = 0.78^{+0.25}_{-0.17} \text{ keV}$, $kT_{\text{high}} = 4.1^{+76}_{-2.3} \text{ keV}$) the overall temperature evolution for SN 1993J with a softening over time is consistent with the spectrum of SN 1979C at this late stage. Since no time-resolved spectroscopy is available for SN 1979C, we used the best-fit spectral template of the *XMM-Newton* MOS data to convert count rates into fluxes, luminosities, and compute mass-loss rates and CSM densities. Changes in the spectral properties, however, do not have a significant impact on the main results from this analysis (see § 2.1).

Chandra data of SN 1998S, which was observed to have a similarly high mass-loss rate ($2 \times 10^{-4} M_{\odot} \text{ yr}^{-1}$) also showed a softening of its spectrum from 10.4 keV at day 678 after its outburst to 8.0 keV on day 1,048 for a thermal plasma fit with Galactic absorption only (Pooley et al. 2002). A more recent *XMM-Newton* observation revealed the emergence of a soft ($\sim 0.8 \text{ keV}$) component, probably from the reverse shock, in addition to the harder component observed with *Chandra* (Immler & Lewin 2003).

In terms of spectral properties, SN 1979C shows a striking resemblance to SN 1978K. At an age of 24.2 yrs, the X-ray spectrum of SN 1978K as observed with *XMM-Newton* was best-fitted with a two-temperature thermal plasma spectrum ($kT_{\text{low}} = 0.61^{+0.04}_{-0.05} \text{ keV}$, $kT_{\text{high}} = 3.16^{+0.44}_{-0.40} \text{ keV}$; Schlegel et al. 2004). Similarly to SN 1979C, SN 1978K shows no decline over the observed period and has been detected at a persistently high X-ray luminosity ($L_{0.5-2} = 1.5 \times 10^{39} \text{ ergs s}^{-1}$), which places both SNe into the category of strongly interacting with dense ambient CSM.

In order to compare the CSM properties in the vicinity of recent SNe for which sufficient data are available, we computed the CSM densities as a function of shell expansion radii for SN 1994I (Immler et al. 2002), SN 1993J (Immler et al. 2001), and SN 1978K (Schlegel et al. 2004) in an identical manner. While the CSM density profiles of SNe 1994I, 1993J, and 1978K can be fitted with a power-law of the form $\rho_{\text{CSM}} = \rho_0(r/r_0)^{-s}$ with $s = 1.9$ (SN 1994I), $s = 1.6$ (SN 1993J), and $s = 1.0$ (SN 1978K), we do not find a statistically acceptable fit for the CSM density profile using all X-ray data of SN 1979C (see Table 3 and Fig. 6). If we only include the *ROSAT* HRI and *XMM-Newton* MOS detection (which have the highest signal-to-noise ratio), we obtain a best-fit CSM density profile of $\rho_{\text{CSM}} = \rho_0(r/r_0)^{-s}$ with $s = 1.6 \pm 1.2$. Inclusion of the early *Einstein* upper limit gives a profile flatter than $s \lesssim 1.7$, consistent with the profile inferred from the *ROSAT* HRI and *XMM-Newton* MOS data. It should be noted, however, that cross-calibration uncertainties of $\lesssim 10\%$ between the *XMM-Newton*, *ROSAT*, and *Einstein* fluxes have not been taken into account, which would increase the error to the CSM profile accordingly (see § 3.1).

While the CSM density profile is flat compared to SNe 1994I and 1993J, it is statistically consistent with a constant mass-loss rate and constant wind velocity profile. Within the errors, the two data points for the *ROSAT* BSPC and *Chandra* measurements are consistent with

¹¹ available at http://xmm.vilspa.esa.es/external/xmm_sw_cal/calib/index.html

the CSM number density inferred from the *ROSAT* HRI and *XMM-Newton* MOS data, and close to the extrapolated CSM density profile of SN 1978K at these large radii from the site of the explosion ($\log r[\text{cm}] = 17.50$ and 17.59 ; see Fig. 6). A higher assumed wind velocity would further decrease the CSM number densities and give an even closer match to the extrapolated SN 1978K profile. Even though clumps in the CSM leading to an increase in the CSM density cannot be conclusively excluded, the seeming ‘jump’ in the CSM density between $\log r[\text{cm}] = 17.67$ (*ROSAT* PSPC) and 17.82 (*Chandra* ACIS data) is likely caused by the large errors associated with the low photon statistics of these observations and cross-calibration uncertainties between the different instruments.

Spatially resolved VLBI radio imaging of SN 1979C at an age of $t = 22$ yrs have, in fact, shown a uniform shell-like structure with no evidence for a clumpy CSM or a geometry different from spherically symmetric (Bartel & Bietenholz 2003). Radio monitoring of SN 1979C over the past decades has shown significant quasi-periodic or sinusoidal modulations in the radio flux (see Fig. 2 in Montes et al. 2000). These modulations in the radio lightcurve have been discussed in the context of a modulation of the stellar wind by a binary companion in a highly eccentric orbit (Weiler et al. 1992; Montes et al. 2000). The lack of a change in the radio spectral index over the monitored period, however, indicates an unchanged emission mechanism with constant efficiency (Montes et al. 2000). Our X-ray data do not support a substantial change in the CSM density profile, but confirm a scenario in which the shock interacts with a dense CSM ($\gtrsim 10^4 \text{ cm}^{-3}$).

4.2. Optical/UV Data

Late-time optical and UV photometry and spectroscopy can yield interesting insights into the CSM properties, such as electron densities, shock velocities and ionization states of the shocked CSM. From these, conclusions can be drawn on the nature and mass of the progenitor, as well as on its evolution. Of particular interest are the late-time optical and UV emission as a result of radiative cooling of the SN shock, ionized by incident X-rays from the CSM shock interaction and by the SN event itself (Chevalier & Fransson 1994).

Multi-band *HST* imaging of the environment of SN 1979C was successfully used to recover optical emission from SN 1979C at $t \approx 20$ yrs after its outburst (van Dyk et al. 1999). The *HST* data showed SN 1979C to be the brightest source at any observed wavelength band (U, B, V, R, I) within a small stellar cluster of red supergiants and young blue stars. While SN 1979C had magnitudes of $m_U = 23.2$ mag, $m_B = 23.3$ mag, $m_V = 22.1$ mag, $m_I = 21.0$ mag, the next brightest optical/UV sources in the environment had $m_V \gtrsim 24$ mag and $m_I \gtrsim 23$ mag. The *HST* images further suggest the presence of 5–7 additional, although faint, UV-emitting stars at the site. Three more UV sources were imaged with the *HST* further to the east ($\approx 2''$), which are located within the OM counts extraction aperture ($2''.9$ radius). It is therefore possible that these sources contribute a significant fraction to the observed optical/UV flux within the extracted aperture.

The new ground-based R -band and $H\alpha$ images taken

in December 2004, some 25.6 yrs after the outburst, continue to indicate a strong CSM interaction, three years after the *XMM-Newton* observations. This suggests that both $H\alpha$ and the broad [O I] and [O II] line emissions seen in the 1993 spectra are still of comparable strength to levels more than a decade earlier.

Little is known to date about the late-time spectra of SNe shortward of $5,000 \text{ \AA}$. UV emission is detected from the position of SN 1979C with a $UVW1$ -band luminosity of $L_{UVW1} = 9 \times 10^{36} \text{ ergs s}^{-1}$. Comparison of the $H\alpha$ and UV luminosities of SN 1979C show an interesting similarity ($L_{H\alpha} = 1.6 \times 10^{37} \text{ ergs s}^{-1}$, van Dyk et al. 1999). The $H\alpha$ lightcurve of SN 1979C shows no decline between 1987 and 1991 (Fesen et al. 1999), while a slight increase in the 1993 data is observed, which coincides with the observed flattening of the radio lightcurve. A similar $H\alpha$ luminosity was observed for the Type II-L SN 1980K ($2.5 \times 10^{37} \text{ ergs s}^{-1}$; Fesen et al. 1999) at an age of 14–15 years after its explosion. These high late-time $H\alpha$ luminosities are largely the result of high electron densities ($n_e \gtrsim 10^4\text{--}10^5 \text{ cm}^{-3}$), which are supported by the high inferred CSM densities in this paper ($\gtrsim 10^4 \text{ cm}^{-3}$).

The OM U -band data show a bright source at the position of SN 1979C ($L_U = 5 \times 10^{36} \text{ ergs s}^{-1}$), while the *HST* data from 1996 show very weak emission from SN 1979C in the U -band. This difference can be attributed to the cut-off of the *HST* U -band filter redward to $3,800 \text{ \AA}$, while the U -band filter of the OM cuts off at $3,950 \text{ \AA}$, which then includes the broad [Ne III] emission lines at $\lambda\lambda 3868, 3869$. The detection of [Ne III] emission lines from SN 1979C (Fesen et al. 1999) may explain why the SN is brighter in the *XMM-Newton* OM U -band images than in the *HST* U -band (F336W filter) images.

The peak surface brightness of the OM U -band emission coincides with the peak in the R -band (see Fig. 7), which includes broad $H\alpha$, [O II] $\lambda\lambda 7319, 7330$, and [O I] $\lambda\lambda 6300, 6364$ line emission from the SN ejecta, and narrow $H\alpha$, presumably associated with the strong CSM interaction. While the source at the position of SN 1979C is classified as point-like in all OM bands by the source detection routines, slightly more extended emission is visible in the OM B and $UVW1$ -band images compared to the U -band. This is consistent with at least a substantial fraction of the B, U ($\lesssim 30\%$) and $UVW1$ -band ($\gtrsim 50\%$) fluxes being to the SN itself. For the $UVW1$ -band, most of the flux likely arises from Mg II $2,800 \text{ \AA}$ where the peak in the $UVW1$ -band effective area is located. A substantial fraction of the B -band flux might also be due to SN 1979C (20–30% contribution to the total light in this OB/SN spatial region) and is due to [O III] $4,363 \text{ \AA}$ line emission. The contribution from the OB stars to the east may be significantly reduced, relative to that from the SN, to the total flux within the U -band passband for both the *HST* and OM filters, due to the Balmer jump at $3,600 \text{ \AA}$ in the stellar spectra of these stars.

Because of the strong appearance of SN 1979C in the OM U -band image, the [Ne III] emission may have substantially increased in strength since the *HST* spectra obtained in 1996 (Fesen et al. 1999). It should be kept in mind, however, that the *HST* data were acquired before the increase of SN 1979C at radio wavelengths. This increase could be caused by either a higher ionization of the CSM interaction and/or a lowering of the local reddening.

ing/extinction due to dust evaporation via shocks (i.e., dust in the CSM) or less ejecta formed dust via dilution from expansion.

In summary, the high inferred optical/UV flux for SN 1979C, especially in the *U*-band, further suggests continued strong CSM interaction even at this late stage in the evolution and large radii from the site of the explosion, which is also supported by our recent MDM *R*-band data, and confirms our results which are independently inferred from the X-ray data.

5. SUMMARY

In this paper we present a comprehensive study of the Type II-L SN 1979C in X-rays and in the optical/UV based on *XMM-Newton* data, all archival X-ray data available to date, as well as archival optical data from the *HST* and a recent MDM observation. Key findings are:

- SN 1979C is observed at a high X-ray luminosity 23 yrs after its outburst ($L_{0.3-2} = 8 \times 10^{38} \text{ ergs s}^{-1}$) and shows no evidence for a decline over the observed period of 16–23 yrs after its outburst.
- The X-ray spectrum, measured for the first time, gives a best-fit two-temperature thermal plasma model with $kT_{\text{high}} = 4.1^{+76}_{-2.3} \text{ keV}$, $kT_{\text{low}} = 0.76^{+0.25}_{-0.17} \text{ keV}$ and Galactic absorption only, characteristic for emission from both the forward (hard component) and reverse shock (soft component). The spectral properties are similar to that of other core-collapse SNe, such as SNe 1978K and 1993J.
- After correction for a decelerating shock front we find no evidence for a change in the progenitor’s mass-loss

rate ($\dot{M} \approx 1.5 \times 10^{-4} M_{\odot} \text{ yr}^{-1}$) over a period of $\gtrsim 16,000$ yrs in the stellar evolution of the progenitor.

- High CSM number densities ($\gtrsim 10^4 \text{ cm}^{-3}$) are inferred for SN 1979C even at large radii (out to $\approx 4 \times 10^{17} \text{ cm}$) from the site of the explosion, similar to SN 1978K. The CSM density profile can be fitted with a power law of the form $\rho_{\text{CSM}} = \rho_0(r/r_0)^{-s}$ with index $s \lesssim 1.7$ comparable to other SNe (e.g., SNe 1994I and 1993J), and support a constant mass-loss rate and a constant stellar wind velocity.

- A point-like optical/UV source is detected at the position of SN 1979C with the Optical Monitor on-board *XMM-Newton*, with *U*, *B*, and *UVW1*-band luminosities of $L_U = 5 \times 10^{36} \text{ ergs s}^{-1}$, $L_B = 7 \times 10^{36} \text{ ergs s}^{-1}$, and $L_{UVW1} = 9 \times 10^{36} \text{ ergs s}^{-1}$, similar to its *H α* and *R*-band luminosity. The high luminosities, especially in the *U*-band arising from Mg II 2,800 Å and in the *UVW1*-band from [Ne III] $\lambda\lambda 3868, 3869$ emission lines, indicate substantial CSM interaction in the late-time evolution of SN 1979C and independently support the strong observed CSM interaction as observed in X-rays.

This paper is based on observations obtained with *XMM-Newton*, an ESA science mission with instruments and contributions directly funded by ESA Member States and NASA. The research has made use of data obtained through the High Energy Astrophysics Science Archive Research Center Online Service, provided by the NASA/Goddard Space Flight Center. KWW wishes to thank the Office of Naval Research (ONR) for the 6.1 funding supporting his research.

REFERENCES

- Bartel, N., Bietenholz, M. F. 2003, *ApJ*, 591, 301
 Chevalier, R. A., Fransson C. 1994, *ApJ*, 420, 268
 Crots, A. P. S. 2001, *BAAS*, 33, 792
 Dickey, J. M., Lockman, F. J. 1990, *ARAA*, 28, 215
 Fesen, R. A., Matonick, D. M. 1993, *ApJ*, 407, 110
 Fesen, R. A., Gerardy, C. L., Filippenko, A. V., Matheson, Th., Chevalier, R. A., Kirshner, R. P., Schmidt, B. P., Challis, P., Fransson, C., Leibundgut, B., van Dyk, S. D. 1999, *A&A*, 117, 725
 Fransson, C. Lundqvist, P. Chevalier, R. A. 1996 *ApJ*, 461, 993
 Freedman, W. L., Madore, B. F., Mould, J.R., et al. 1994, *Nat* 371, 757
 Immler, S., Pietsch, W., Aschenbach, B. 1998, *A&A*, 331, 601
 Immler, S., Aschenbach, B., Wang, Q. D., 2001, *ApJ*, 561, L107
 Immler, S., Wilson, A. S., Terashima, Y., 2002, *ApJ*, 573, L27
 Immler, S., Lewin, W. 2003, in *Supernovae and Gamma-Ray Bursters* (ed K. Weiler), *Lecture Notes in Physics*, 598, 91
 Johnson, G. E. 1979, *IAU Circ.*, No. 3348
 Kaaret, P. 2001, *ApJ*, 560, 715
 Marcaide, J. M., Pérez-Torres, M. A., Ros, E., Alberdi, A., Diamond, P. J., Guirado, J. C., Lara, L., Van Dyk, S. D., Weiler, K. W. 2002, *A&A*, 384, 408
 Montes, M. J., Weiler, K. W., Van Dyk, S. D., Panagia, N., Lacey, Ch. K., Sramek, R. A., Park, R. 2000, *ApJ*, 532, 1124
 Pooley D., Lewin, W. H. G., Fox, D. W., et al. 2002, *ApJ*, 572, 932
 Ray, A., Petre, R., Schlegel, E. M. 2001, *AJ*, 122, 966
 Schlegel, E. M., Ryder, S., Staveley-Smith, L., Petre, R., Colbert, E., Dopita, M., Campbell-Wilson, D. 1999, *AJ*, 118, 2689
 Schlegel, E. M., Kong, A., Kaaret, P., DiStefano, R., Murray, S. 2004, *ApJ*, 603, 644
 Snowden, S. L. 2002, in *ESTEC Symposium 'New Visions of the X-ray Universe in the XMM-Newton and Chandra Era'*, 26–30 November 2001 (astro-ph/0203311)
 Sramek, R. A., Weiler, K. W. 2003, in *Supernovae and Gamma-Ray Bursters* (ed K. Weiler), *Lecture Notes in Physics*, 598, 145
 van Dyk, S. D., Weiler, K. W., Sramek, R. A., Rupen, M. P., Panagia, N. 1994, *ApJ*, 432, L115
 van Dyk, S. D., Peng, C. Y., Barth, A. J., Filippenko, A. V., Chevalier, R. A., Fesen, R. A., Fransson, C., Kirshner, R. P., Leibundgut, B. 1999, *PASP*, 111, 313
 Weiler, K. W., Sramek, R. A., Panagia, N., van der Hulst, J. M., Salvati, M. 1986, *ApJ*, 301, 790
 Weiler, K. W., van Dyk, S. D., Discenna, J. L., Panagia, N., Sramek, R. A. 1991, *ApJ*, 380, 161
 Weiler, K. W., van Dyk, S. D., Pringle, J. E., Panagia, N. 1992, *ApJ*, 399, 672
 Weiler, K. W., Panagia, N., Sramek, R. A., van Dyk, S. D., Montes, M. J., Lacey, Ch. K. 2001, in *Supernovae and Gamma-Ray Bursts* (eds M. Livio, N. Panagia, K. Sahu), Cambridge University Press, Vol 12, 198
 Zimmermann, H.-U., Aschenbach, B. 2003, *A&A*, 406, 969

TABLE 1
X-RAY OBSERVATIONS OF SN 1979C

Mission	Instrument	Obs-ID/Seq-No	Date	Exposure	MJD
<i>Einstein</i>	HRI	H1220N16.XIA	1979-06-07	4.0 ks	44,031
<i>Einstein</i>	HRI	H1220N16.XIB	1979-12-12	13.4 ks	44,217
<i>Einstein</i>	HRI	H1220N16.XIC	1980-06-29	23.8 ks	44,418
<i>ROSAT</i>	HRI	RH600731N00	1995-06-17	42.8 ks	49,885
<i>ROSAT</i>	HRI	RH500422N00	1995-07-01	9.0 ks	49,899
<i>ASCA</i>	SIS	55044000	1997-12-24	27.3 ks	50,806
<i>ROSAT</i>	HRI	RH500542N00	1997-12-27	25.1 ks	50,809
<i>ROSAT</i>	PSPC	RP180296N00	1998-12-08	7.8 ks	51,155
<i>Chandra</i>	ACIS-S	400	1999-06-11	2.5 ks	51,340
<i>XMM-Newton</i>	MOS	0106860201	2001-12-28	36.6 ks	52,271

NOTE. — All *Einstein* HRI observations were merged into a single 41.2 ks observation.

TABLE 2
OPTICAL/UV OBSERVATIONS OF SN 1979C

Telescope	Filter	Date	Exposure	MJD
<i>HST</i> WFPC2-PC1	U (F336W)	1996-07-29	2.6 ks	50,293
<i>HST</i> WFPC2-PC1	B (F439W)	1996-07-29	2.4 ks	50,293
<i>HST</i> WFPC2-PC1	R (F675W)	1996-07-29	1.0 ks	50,293
<i>HST</i> WFPC2-PC1	H α (F658W)	1996-07-29	3.9 ks	50,293
<i>XMM-Newton</i> OM	U	2001-12-28	1.8 ks	52,271
<i>XMM-Newton</i> OM	B	2001-12-28	2.0 ks	52,271
<i>XMM-Newton</i> OM	UVW1	2001-12-28	1.9 ks	52,271
MDM Hiltner 2.4m	R	2004-12-19	2.0 ks	53,358
MDM Hiltner 2.4m	H α	2004-12-19	3.0 ks	53,358

TABLE 3
X-RAY PROPERTIES OF SN 1979C

Epoch [yrs]	Instrument	$f_{0.3-2}$ [10^{-14} ergs cm $^{-2}$ s $^{-1}$]	$L_{0.3-2}$ [10^{39} ergs s $^{-1}$]	\dot{M} [$10^{-4} M_{\odot}$ yr $^{-1}$]	$\log r$ [cm]	t_w [yrs]	n [10^4 cm $^{-3}$]
(1)	(2)	(3)	(4)	(5)	(6)	(7)	(8)
0.66	<i>Einstein</i> HRI	< 12.78	< 4.47	< 0.71	16.28	615	< 223.87
16.18	<i>ROSAT</i> HRI	2.20 ± 0.37	0.77 ± 0.13	1.45 ± 0.25	17.50	14,878	1.17 ± 0.32
16.22	<i>ROSAT</i> HRI	< 5.09	< 1.78	< 2.19	17.51	14,914	< 1.17
18.71	<i>ASCA</i> SIS	< 4.92	< 1.72	< 2.33	17.51	17,200	< 1.66
18.72	<i>ROSAT</i> HRI	< 5.15	< 1.80	< 2.36	17.51	17,208	< 1.66
19.67	<i>ROSAT</i> PSPC	2.21 ± 0.63	0.77 ± 0.22	1.62 ± 0.46	17.52	18,080	1.66 ± 0.63
20.17	<i>Chandra</i> ACIS-S	2.23 ± 0.71	0.78 ± 0.25	1.63 ± 0.52	17.53	18,546	1.51 ± 0.56
22.72	<i>XMM-Newton</i> MOS	2.31 ± 0.26	0.81 ± 0.09	1.75 ± 0.19	17.59	20,893	0.85 ± 0.19

NOTE. — (1) Epoch after the peak optical brightness (April 15, 1979) in units of yrs; (3) 0.3–2 keV X-ray band flux in units of ergs cm $^{-2}$ s $^{-1}$; (4) 0.3–2 keV X-ray band luminosity in units of ergs s $^{-1}$; (5) mass-loss rate of the progenitor in units of M_{\odot} yr $^{-1}$; (6) log of the radius from the site of the explosion; (7) age of the stellar wind in units of yrs; (8) post-shock CSM number density in units of 10^4 cm $^{-3}$.

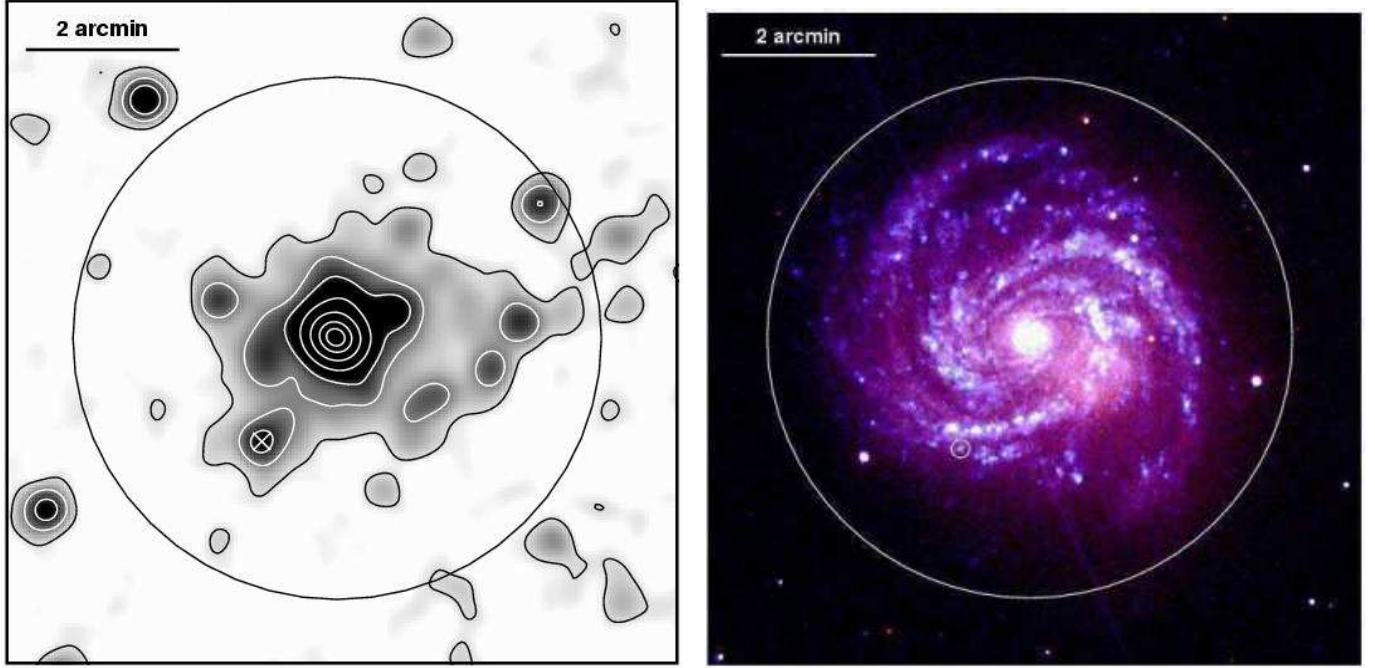


FIG. 1.— **Left-hand panel:** Merged XMM-Newton EPIC MOS1+MOS2 image of M100 and SN 1979C in the 0.3–10 keV band in logarithmic gray-scale. The image was adaptively smoothed to achieve a signal-to-noise ratio of 10. Contour lines are 0.65 (black), 1, 1.5, 3, 6, 10, and 13×10^{-5} cts s $^{-1}$ pix $^{-1}$. The position of SN 1979C is marked by a white cross. The black circle gives the D_{25} ellipse of M100. **Right-hand panel:** B (red), U (green), and $UVW1$ (blue) Optical Monitor image of M100. The small white circle (radius $7''.5$) is centered on the radio position of SN 1979C. The large white circle indicates the D_{25} ellipse of M100 as in the left-hand panel.

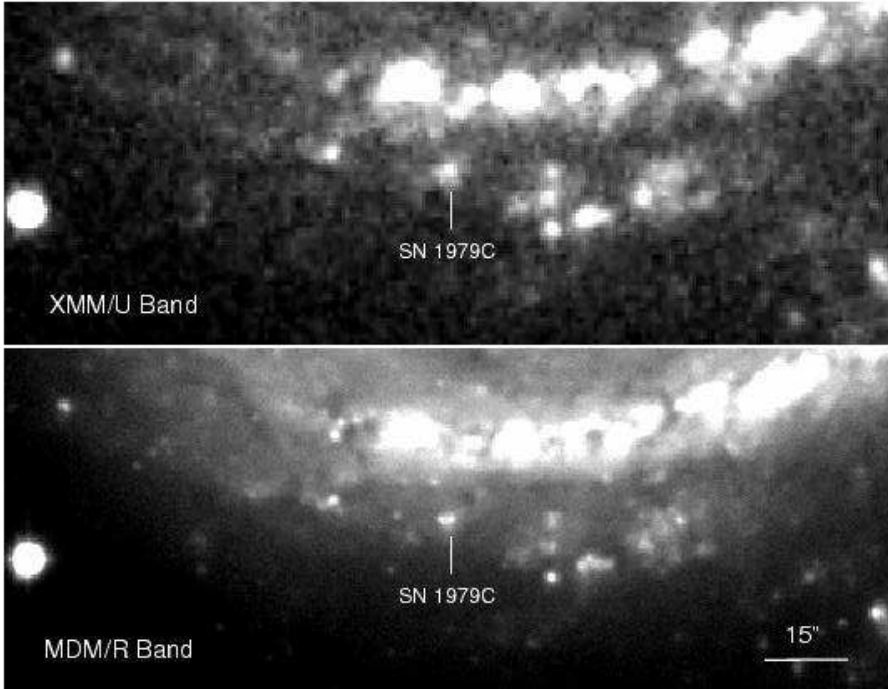


FIG. 2.— XMM-Newton Optical Monitor U -band image (upper panel) and MDM 2.4-m Hiltner Telescope R -band image of the southern spiral arm of M100 centered on the position of SN 1979C. The $15''$ scalebar in the lower panel applies to both panels.

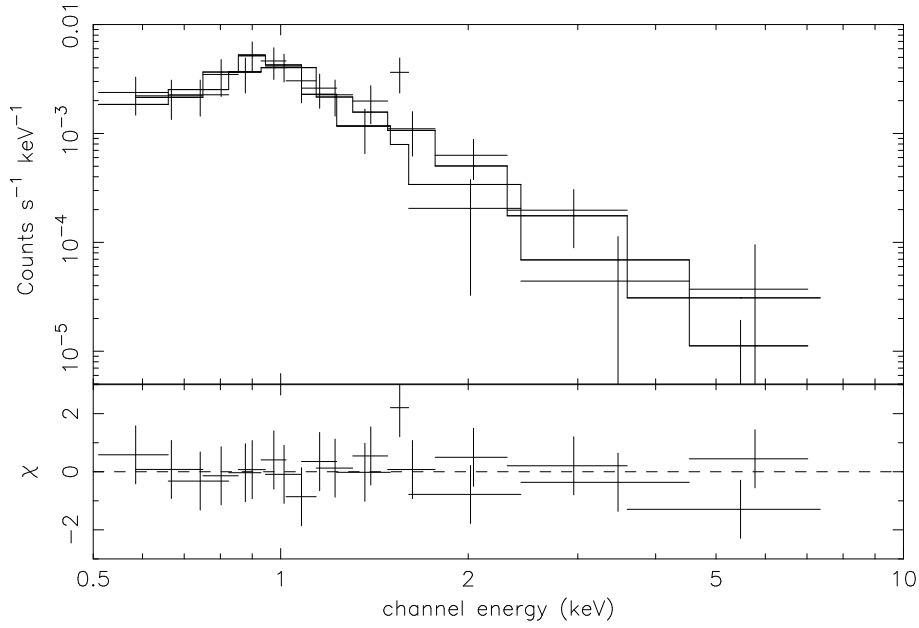


FIG. 3.— EPIC MOS1 and MOS2 X-ray spectra of SN 1979C (upper panel). The lower panel shows the residuals of the fits in units of σ for the best-fit spectral model consisting of a two-component thermal plasma emission model (see §3.1).

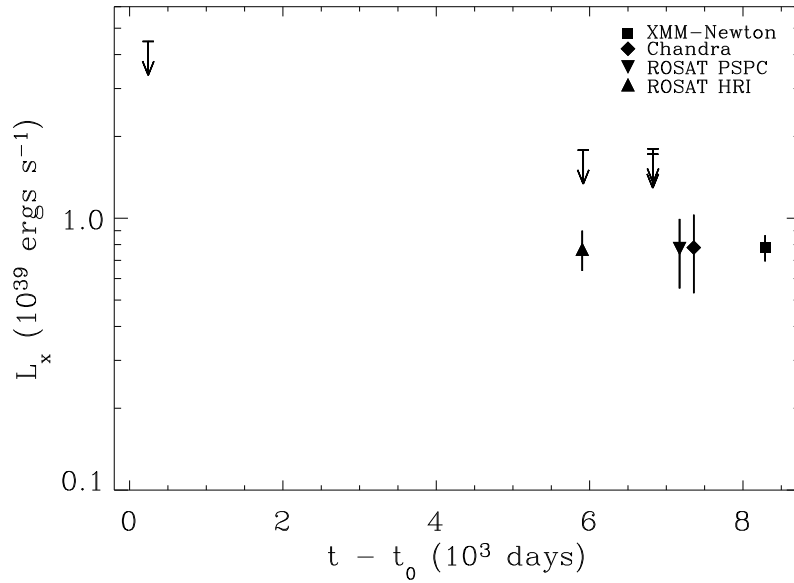


FIG. 4.— Soft (0.3–2 keV) band X-ray lightcurve of SN 1979C based on *Einstein*, *ROSAT*, *ASCA*, *Chandra*, and *XMM-Newton* data. Upper limits are from *Einstein* HRI, *ROSAT* HRI and *ASCA* SIS observations. Time is given in units of 10^3 days after the outburst of SN 1979C (see Table 1).

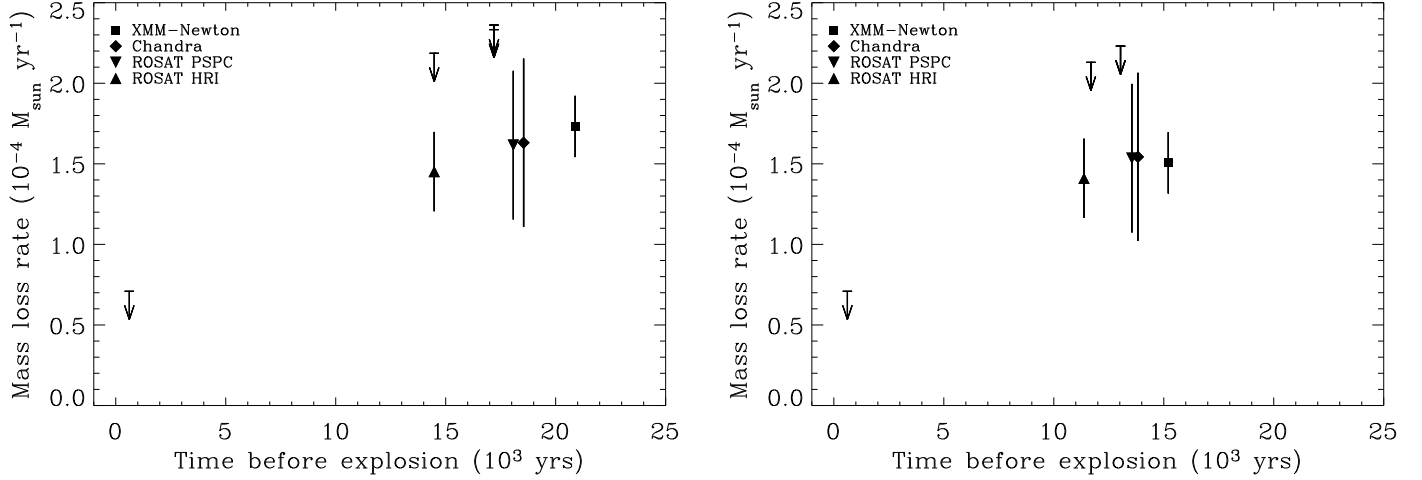


FIG. 5.— **Left-hand panel:** Mass-loss rate history of SN 1979C as a function of the stellar wind age in units of 10^3 years before the explosion for a constant shock velocity (see Table 1 and §3). **Right-hand panel:** Mass-loss rate history of SN 1979C as a function of the stellar wind age in units of 10^3 years before the explosion for a decelerated shock (see §3.1).

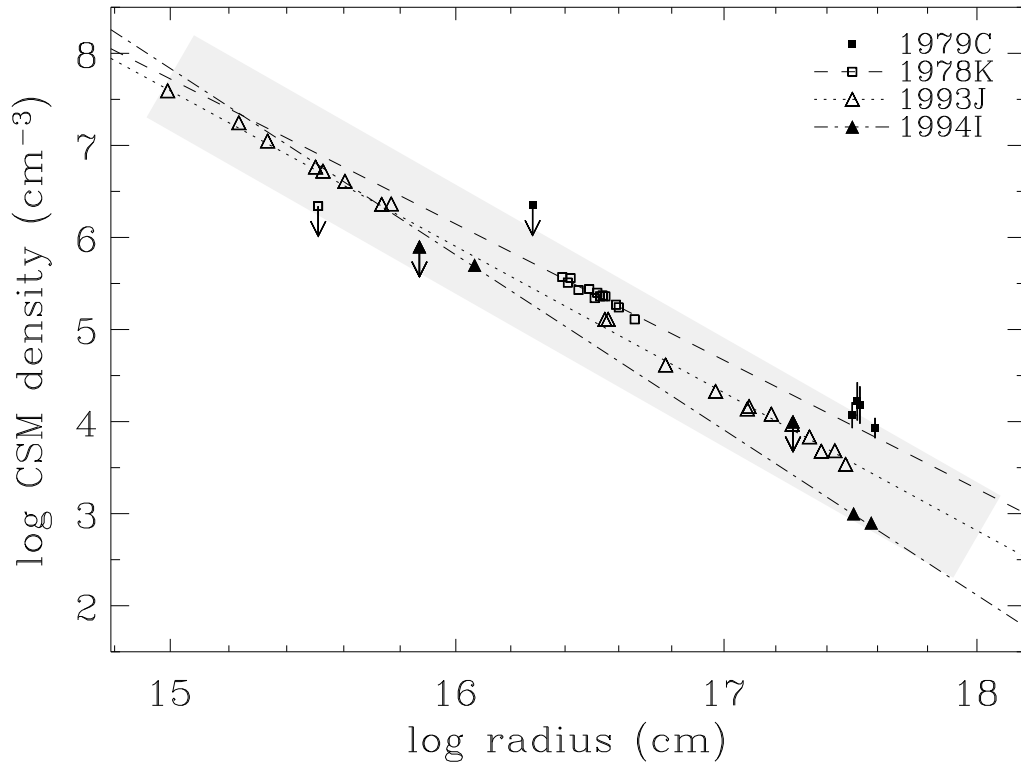


FIG. 6.— Circumstellar matter density profiles as a function of SN shell expansion radii for SNe 1994I (filled triangles; Immler et al. 2002), 1993J (open triangles; Immler et al. 2001), 1978K (open box; this work), and 1979C (filled box; this work). Error bars for SN 1979C are $\pm 1\sigma$. Best-fit CSM density profiles of $\rho_{\text{CSM}} \propto r^{-s}$ with indices $s = -1.9$ (SN 1994I), $s = -1.6$ (SN 1993J), and $s = -1.0$ (SN 1978K) are drawn as lines.

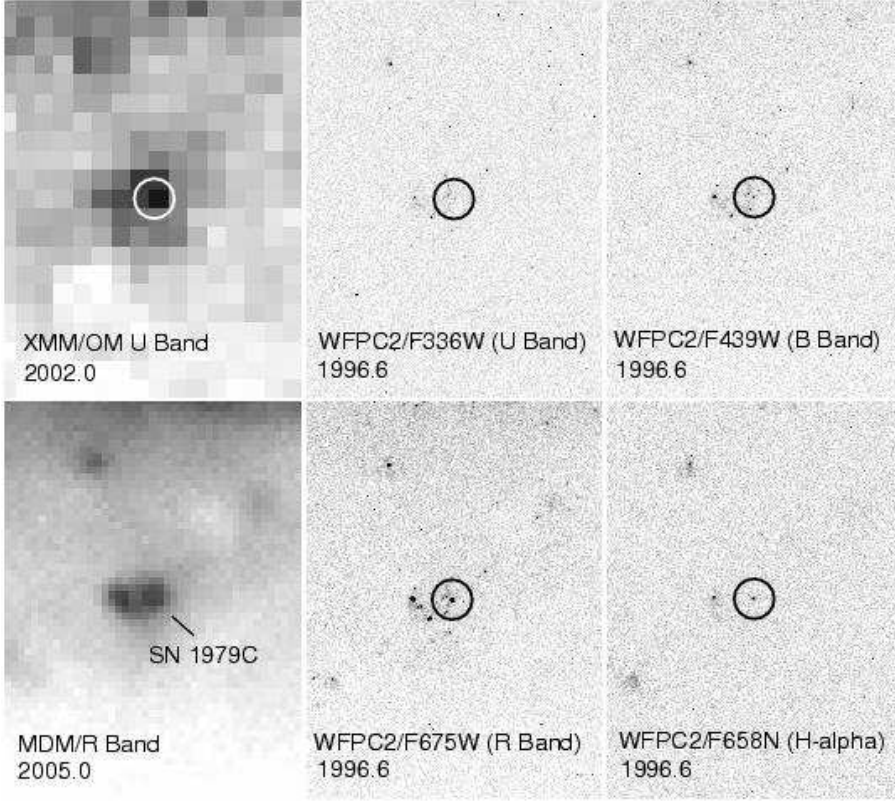


FIG. 7.— *XMM-Newton* OM *U*-band image (from December 28, 2001; upper left-hand panel), MDM *R*-band image (from December 19 and 20, 2004; lower left-hand panel), and *HST* WFPC2-PC1 *U*, *B*, *R*-band and $H\alpha$ images (from July 29, 1996; middle and right-hand panels) of the SN 1979C region. The circles (radius $1''$) are at the *HST* *R*-band centroid position of SN 1979C.